



**HAL**  
open science

# Antimony isotope fractionation during Sb(V) and Sb(III) adsorption on secondary Fe-minerals (schwertmannite, ferrihydrite) typical of mine waters

Colin Ferrari, Eléonore Resongles, Rémi Freydier, Corinne Casiot

## ► To cite this version:

Colin Ferrari, Eléonore Resongles, Rémi Freydier, Corinne Casiot. Antimony isotope fractionation during Sb(V) and Sb(III) adsorption on secondary Fe-minerals (schwertmannite, ferrihydrite) typical of mine waters. *Applied Geochemistry*, 2024, 163, 105935 [11 p.]. 10.1016/j.apgeochem.2024.105935 . hal-04735865

**HAL Id: hal-04735865**

**<https://hal.science/hal-04735865v1>**

Submitted on 14 Oct 2024

**HAL** is a multi-disciplinary open access archive for the deposit and dissemination of scientific research documents, whether they are published or not. The documents may come from teaching and research institutions in France or abroad, or from public or private research centers.

L'archive ouverte pluridisciplinaire **HAL**, est destinée au dépôt et à la diffusion de documents scientifiques de niveau recherche, publiés ou non, émanant des établissements d'enseignement et de recherche français ou étrangers, des laboratoires publics ou privés.

1 Antimony isotope fractionation during Sb(V) and Sb(III) adsorption  
2 on secondary Fe-minerals (schwertmannite, ferrihydrite) typical of  
3 mine waters

4

5 *Colin Ferrari<sup>a</sup>, Eléonore Resongles<sup>\*a</sup>, Rémi Freydier<sup>a</sup>, and Corinne Casiot<sup>a</sup>*

6

7 <sup>a</sup>HydroSciences Montpellier, Univ. Montpellier, CNRS, IRD, Montpellier, France

8 **\*Corresponding author:**

9

Mailing address: Université Montpellier – HydroSciences

10

Bâtiment HYDROPOLIS

11

15 avenue Charles Flahault

12

34090 Montpellier

13

Email: [eleonore.resongles@ird.fr](mailto:eleonore.resongles@ird.fr)

15           The application of antimony (Sb) isotopes as tracers for Sb environmental cycling is  
16 currently limited. Indeed, there is a lack of knowledge of isotope fractionation factors  
17 associated with key (bio-) geochemical processes controlling its behaviour in surface  
18 environments. This study investigated the equilibrium isotope fractionation generated by  
19 Sb(V) and Sb(III) sorption on two iron minerals typical of acid mine drainage (AMD)  
20 impacted streams, ferrihydrite and schwertmannite, under controlled conditions of pH and  
21 solid to liquid ratio. Sorption behaviour and Sb isotope fractionation were similar for the  
22 different mineral phases and Sb oxidation degrees, with fractionation factors  $\Delta^{123}\text{Sb}_{\text{solid-solution}}$   
23 of  $-0.25 \pm 0.08 \text{ ‰}$  for Sb(III) and  $-0.34 \pm 0.08 \text{ ‰}$  for Sb(V) adsorbed on ferrihydrite and -  
24  $0.36 \pm 0.06 \text{ ‰}$  for Sb(III) and  $-0.27 \pm 0.03 \text{ ‰}$  for Sb(V) adsorbed on schwertmannite. The pH  
25 and initial Fe:Sb ratio did not significantly affect the  $\Delta^{123}\text{Sb}_{\text{solid-solution}}$  value under the  
26 experimental conditions. The light  $^{121}\text{Sb}$  isotope was preferentially adsorbed on the mineral  
27 phases, following an equilibrium closed system between dissolved and adsorbed Sb species.  
28 This fractionation may be related to the apparition of iron as the second closest neighbour  
29 which distorts the  $\text{Sb}(\text{OH})_3$  or  $\text{Sb}(\text{OH})_6^-$  atomic polyhedron. This study confirms that Sb  
30 equilibrium isotope fractionation occurs during sorption of Sb(III) and Sb(V) onto secondary  
31 iron minerals and suggests that the pH and redox of Sb do not exert significant effect. pH and  
32 redox conditions are important parameters which control Sb mobility in AMD streams,  
33 therefore, the study provides data for interpreting Sb isotope signatures in mine waters.

34

35 Keywords : Antimony isotopes – Equilibrium isotope fractionation – Iron oxyhydroxides –  
36 Adsorption – Mining Environments

37

38 1. INTRODUCTION

39 Antimony (Sb) is a critical element for the modern industry, mainly for its application as a  
40 flame retardant in plastics and its use in lead alloys (European Commission, 2020; U.S.  
41 Geological Survey, 2022). As a consequence, Sb mine production has peaked over the last  
42 twenty years with an annual world production of 142 to 193 kT (2004-2018 data, U.S.  
43 Geological Survey, 2018) leading to a general increase of Sb levels in the environment (He *et al.*,  
44 2019; Bolan *et al.*, 2022). In surface waters, dissolved Sb concentrations are usually low  
45 ( $< 1 \mu\text{g.L}^{-1}$ ) and the highest concentrations of this toxic element (up to  $\sim 29 \text{ mg.L}^{-1}$ ) are found  
46 in streams in sulphide mining areas (Wang *et al.*, 2011; Guo *et al.*, 2018; Hao *et al.*, 2021).

47 In mining Sb-rich environments, the alteration of sulphides produces acid leachates (acid  
48 mine drainage, AMD), that contain high concentrations of iron and sulphate. These  
49 constituents precipitate subsequently to iron oxidation and AMD neutralization by river water;  
50 they form secondary minerals, hydrous ferric oxides (HFO) and ferric hydroxysulphates  
51 (Bigham *et al.*, 1996). Due to their high specific surface area and positive surface charges,  
52 these minerals are good sorbents for antimony (Leuz *et al.*, 2006; Mitsunobu *et al.*, 2006;  
53 Mitsunobu *et al.*, 2010; Guo *et al.*, 2014; Qi and Pichler, 2016, 2017; Schoepfer *et al.*, 2021)  
54 and therefore, they control the transport of Sb in the rivers receiving mining effluents (Filella,  
55 Williams and Belzile, 2009; Manaka *et al.*, 2007; Nagano *et al.*, 2011; Resongles *et al.*, 2013;  
56 Johnston *et al.*, 2020, Rastegari *et al.*, 2022, Shan *et al.*, 2023). Among the solid phases most  
57 commonly encountered in AMD streams and downstream rivers, are schwertmannite  
58 ( $\text{Fe}_8\text{O}_8(\text{OH})_{8-2x}\text{SO}_{4x} \cdot n\text{H}_2\text{O}$ ,  $1 < x < 1.75$ ) in the pH range 2-4.5 and ferrihydrite  
59 ( $\text{Fe}_5\text{HO}_8, 4\text{H}_2\text{O}$ ) at  $\text{pH} \geq 6.5$  (Bigham *et al.*, 1996; Schoepfer *et al.*, 2021). The oxidative  
60 dissolution of stibnite ( $\text{Sb}_2\text{S}_3$ ), the main Sb ore, can lead to the release of Sb in water in its  
61 trivalent form, Sb(III) (Biver and Shotytk, 2012). Besides oxidation, attenuation of dissolved  
62 Sb(III) concentrations in mine waters is attributable to Sb(III) adsorption on Fe secondary  
63 minerals (Beauchemin *et al.*, 2012; Resongles *et al.*, 2013). These field observations were  
64 further supported by experimental adsorption studies which showed that Sb(III) is more  
65 efficiently adsorbed on ferrihydrite and schwertmannite than Sb(V) (Qi and Pichler, 2016; Li  
66 *et al.*, 2016).

67 Antimony isotope system ( $^{121}\text{Sb}$  and  $^{123}\text{Sb}$ ) is emerging due to its strong potential as a  
68 geochemical tracer (Teng *et al.*, 2017; Johnson *et al.*, 2022). Several studies were focused on  
69 sample preparation and optimization of Sb isotope ratio analysis by Multi Collector  
70 Inductively Coupled Plasma Mass Spectrometry MC-ICP-MS (Asaoka *et al.*, 2011; Lobo *et*

71 *al.*, 2012; Liu *et al.*, 2020; Kaufmann *et al.*, 2021; Ferrari *et al.*, 2021; Li *et al.*, 2021; Sun *et*  
72 *al.*, 2021). Others provided data on Sb isotope signatures in primary Sb minerals,  
73 manufactured materials and environmental samples (Rouxel *et al.*, 2003; Lobo *et al.*, 2013,  
74 2014; Degryse *et al.*, 2015, 2020; Resongles *et al.*, 2015; Ferrari *et al.*, 2021). However, to  
75 date Sb isotope fractionation factors associated with geochemical processes such as adsorption  
76 are poorly known, limiting the development of Sb isotopes as environmental tracers.

77 The extent of isotope fractionation occurring during metal sorption generally remains  
78 limited ( $< 1 \%$ ) (Wiederhold, 2015; Komárek *et al.*, 2021). Both light and heavy isotope  
79 enrichments in adsorbed species have been observed in metal sorption studies on  
80 oxyhydroxides, depending on the bonding environment of adsorbed and aqueous metal  
81 species (Komárek *et al.*, 2021). Isotope fractionation generated by sorption also varies with  
82 the mineralogy (Komárek *et al.*, 2021), for example in the case of the sorption of Zn adsorbed  
83 on ferrihydrite and goethite (Juillot *et al.*, 2008), of Mo on Fe-(oxyhydr)oxides, for which the  
84 fractionation increases in the order magnetite  $<$  ferrihydrite  $<$  goethite  $<$  hematite (Goldberg *et*  
85 *al.*, 2009), or Sb(V) adsorbed on alumina  $<$  ferrihydrite  $<$  hematite and goethite (Zhou *et al.*,  
86 2022, 2023). This mineral effect can be related both to mineral surface speciation and solution  
87 chemistry (Goldberg *et al.*, 2009). A number of studies showed that the outer-sphere  
88 complexation generates lower fractionation than the inner-sphere complexation due to the  
89 control of complexing ligands by weak electrostatic forces on the surface and their  
90 participation in anion exchange (Essington and Stewart, 2018). The inner-sphere  
91 complexation is subject to stronger bonding (Essington and Stewart, 2018; Zhou *et al.*, 2022,  
92 2023). Therefore, the bonding environment of Sb in the solid and aqueous phases is of prime  
93 interest to interpret the observed Sb isotope fractionation factors. Antimony adsorption  
94 mechanisms have been investigated at the molecular level on various iron minerals including  
95 ferrihydrite, schwertmannite, hematite and goethite (Scheinost *et al.*, 2006; Mitsunobu *et al.*,  
96 2010; Guo *et al.*, 2014; Essington and Stewart, 2018; Zhou *et al.*, 2023; Shan *et al.*, 2023).  
97 Antimony(V) forms inner-sphere complexes at the surface of ferrihydrite by edge-sharing and  
98 edge and corner-sharing independently from pH or surface coverage (Mitsunobu *et al.*, 2010;  
99 Guo *et al.*, 2014; Zhou *et al.*, 2023). For schwertmannite, Sb adsorption studies have mainly  
100 focused on its use as a sorbent for the treatment of water contaminated with Sb (Schoepfer *et*  
101 *al.*, 2021). An experimental and modeling study suggested the formation of inner-sphere  
102 complexes between Sb(V) and schwertmannite (Nagano *et al.*, 2011). This was recently  
103 confirmed by a study at the molecular scale revealing edge-sharing and corner-sharing  
104 complexation between Sb(V) and schwertmannite accompanied by its incorporation in the

105 mineral structure depending on pH and Sb loading (Shan et al., 2023). Recently, two  
106 experimental studies (Zhou *et al.*, 2022, 2023) focused for the first time on Sb isotope  
107 fractionation during sorption on aluminium and iron oxy(hydro)xides. The authors found that  
108 Sb(V) adsorption on aluminium oxides does not produce significant equilibrium Sb isotope  
109 fractionation (Zhou et al., 2022). On the other hand, a significant equilibrium isotope  
110 fractionation was observed as a result of Sb(V) adsorption on ferrihydrite, hematite and  
111 goethite ( $-1.14\text{ ‰} < \Delta^{123}\text{Sb}_{\text{solid-solution}} < -0.49\text{ ‰}$ ). The difference in the magnitude of the  
112 fractionation factors among the three Fe minerals was ascribed to different inner-sphere  
113 adsorption mechanisms of Sb(V) on ferrihydrite (formation of edge and corner-sharing  
114 complexes) and hematite or goethite (formation of edge-sharing complexes) (Zhou *et al.*,  
115 2023). Therefore, these pioneering studies evidenced that the extent of Sb isotope  
116 fractionation generated by adsorption depends on the mineral phases and Sb adsorption modes  
117 as previously reported for other elements such as Cd, Cu, Ni, Se or Zn (Xu *et al.*, 2020;  
118 Komárek *et al.*, 2021).

119 Antimony isotope fractionation generated by adsorption processes needs further  
120 investigation to quantify fractionation factors involving other environmentally relevant  
121 mineral phases and Sb(III) species. In particular, in the perspective of using Sb isotopes to  
122 track pollution sources in watersheds impacted by sulphide ore mining, and/or to unravel the  
123 processes Sb undergoes in mine-impacted streams, it is essential to document Sb isotope  
124 fractionation during sorption of Sb(III) and Sb(V) on secondary iron minerals typical of AMD  
125 streams.

126 In this context, the objective of this study was to complement recent studies by focusing on  
127 the quantification of the isotope fractionation factors at equilibrium between dissolved and  
128 adsorbed Sb species, both in a trivalent and pentavalent Sb form, on two mineral phases  
129 widely distributed in sulphide mining environments, ferrihydrite and schwertmannite, and to  
130 make hypothesis regarding the possible origin of the observed fractionation based on existing  
131 knowledge on adsorption mechanisms.

132

133

134 2. MATERIAL AND METHODS

135 2.1. Reagents and materials

136 Ultrapure water (Milli-Q®, resistivity > 18.2 MΩ.cm, Q-POP Element system,  
137 Millipore) was used for all experiments and reagent preparation. All consumables (e.g.,  
138 sample bottles, tubes, SPE cartridge, pipette tips...) were soaked in 10 % w/w analytical grade  
139 HCl for 48 h and rinsed three times with ultrapure water before use. Fe(NO<sub>3</sub>)<sub>3</sub>·9H<sub>2</sub>O (Sigma-  
140 Aldrich®), FeSO<sub>4</sub>·7H<sub>2</sub>O (Sigma-Aldrich®), 30 % w/w H<sub>2</sub>O<sub>2</sub> (analytical grade, Fisher  
141 Scientific®), 1 mol.L<sup>-1</sup> KOH (Merck®) were used for the synthesis of schwertmannite and 2-  
142 line ferrihydrite. NaNO<sub>3</sub> (Merck®) and NaOH (99.99 % trace metal basis, Sigma-Aldrich®)  
143 were used for adsorption experiments. 30 % w/w HCl (Suprapur, Merck®), 65–69 % w/w  
144 HNO<sub>3</sub> (Analpure, Analytika®), ascorbic acid (analytical grade, Sigma-Aldrich®), KI  
145 (Suprapur, Merck®) and NaBH<sub>4</sub> (99.99 % trace metal basis, Sigma-Aldrich®) were used for  
146 sample preparation for Sb concentration and isotope analyses. Ethylenediaminetetraacetic acid  
147 disodium salt (EDTA, analytical grade, J. T. Baker®) and potassium hydrogen-phthalate  
148 (KHP, SigmaUltra, 99.95 %, Sigma-Aldrich) were used to prepare the eluent for Sb speciation  
149 analysis. Acetic acid (Suprapur, Merck®) and EDTA (analytical grade, J. T. Baker®) were  
150 used as additive for preserving Sb redox species in samples during Sb redox speciation  
151 analysis. Stock solutions of Sb(V) and Sb(III) at 1 g.L<sup>-1</sup> were prepared separately by  
152 dissolving an appropriate amount of potassium hexahydroxoantimonate(V) (KSb(OH)<sub>6</sub>,  
153 analytical grade, Merck®) and potassium antimony(III) oxide tartrate hemihydrates  
154 (K(SbO)C<sub>4</sub>H<sub>4</sub>O<sub>6</sub>·0.5H<sub>2</sub>O, Extrapure, Merck®) in ultrapure water. Antimony concentration in  
155 Sb(V) and Sb(III) stock solutions were checked by ICP-MS. These solutions were used for  
156 preparing calibration solutions for Sb speciation analysis (separate calibration solutions for  
157 Sb(V) and Sb(III)) and for adsorption experiments. It is noteworthy that Sb(III) standard  
158 solution contained a small proportion of Sb(V). Therefore, Sb(V) was quantified in Sb(III)  
159 calibration standard solutions to correct Sb(III) concentrations of the calibration curve. In  
160 addition, it should be noted that Sb(III) adsorption experiments also contained ~2 % of Sb(V)  
161 at the beginning. This was taken into account in verifying the absence of oxidation during  
162 sorption experiments with Sb(III). The mono-elemental Sb SPEX standard solution (1000 µg  
163 mL<sup>-1</sup> in 20 % w/w HCl, batch number 24-175SBX, SPEX CertiPrep) was used as Sb isotopic  
164 standard (Ferrari *et al.*, 2021).

165 All experiments were carried out in a lab with controlled temperature conditions ( $20 \pm$   
166  $1 \text{ }^\circ\text{C}$ ). Sample dilutions and preparation for ICP-MS and HG-MC-ICP-MS analyses were  
167 carried out in class 10 000 cleanroom facility.

## 168 2.2. Ferrihydrite and schwertmannite synthesis and characterization

169 Two-line ferrihydrite was synthesized following the protocol of Schwertmann and Cornell  
170 (2000) and schwertmannite was synthesized following the protocol of Liu *et al.*, (2015)  
171 adapted from Regenspurg *et al.*, (2004). Details of the procedures are given in Appendix  
172 (Section 1). The quality of the synthesized ferrihydrite and schwertmannite was checked  
173 using XRD (X-ray powder diffraction), BET (Brunauer-Emmett-Teller) and SEM (Scanning  
174 Electron Microscopy, schwertmannite only) analysis (PAC and MEA platforms, Université de  
175 Montpellier). The methods and results are briefly presented in Appendix (Section 1, Figure  
176 A1 and A2).

## 177 2.3. Sorption experiments

178 Sorption experiments were conducted at different pH and initial Fe:Sb ratios. Every  
179 condition was made in duplicate or triplicate to check the reproducibility of the experiment.  
180 Intermediate suspensions of ferrihydrite or schwertmannite were prepared at  $1 \text{ g.L}^{-1}$  and  
181 agitated for 48 h before the experiment to ensure homogeneity. Then, suspensions (50 mL)  
182 containing  $0.01 \text{ g.L}^{-1}$  of ferrihydrite or schwertmannite in a  $0.01 \text{ M NaNO}_3$  electrolyte were  
183 prepared in HDPE bottles and after a pH adjustment step, the suspensions were doped with  
184 Sb(III) or Sb(V) to reach a final Sb concentration of 0.1, 0.5, 1 and  $10 \text{ mg.L}^{-1}$ . As a result, the  
185 initial Fe:Sb molar ratios were 144, 29, 14 and 1.4 for Sb(III) adsorption experiment on  
186 ferrihydrite, 126, 25, 13 and 1.3 for Sb(V) adsorption experiment on ferrihydrite and 120, 24,  
187 12 and 1.2 for Sb(III) and Sb(V) adsorption experiments on schwertmannite. In addition,  
188 procedural blanks containing ferrihydrite or schwertmannite were prepared and treated as  
189 samples to ensure that no contamination occurred at any step of the experiment. Finally,  
190 bottles were wrapped in an aluminium sheet and agitated at 300 rpm on a stirring table for 48  
191 h at  $20 \pm 1 \text{ }^\circ\text{C}$ .

192 The pH of the suspensions was adjusted to correspond to the stability domain of ferrihydrite  
193 and schwertmannite observed in natural waters impacted by mine drainage (Bigham *et al.*,  
194 1996). The pH was thus fixed at 6, 7 and 8 for ferrihydrite and 2.5 and 4.5 for schwertmannite  
195 using  $0.1 \text{ M NaOH}$  and  $0.1 \text{ M HCl}$ , respectively. The pH was monitored twice a day and re-  
196 adjusted when needed.



197 Sacrifices of the suspensions were carried out after 48 h, after chemical and isotopic  
198 equilibrium had been reached. This equilibrium time was defined based on preliminary kinetic  
199 monitoring for Sb(V) sorption on ferrihydrite and for Sb(III) and Sb(V) sorption on  
200 schwertmannite (Appendix, Table A1, Figure A3). Chemical equilibrium was reached in less  
201 than 48 h for all tested conditions and both minerals. These results were consistent with the  
202 literature regarding Sb sorption on ferrihydrite under conditions similar to the present study  
203 (initial Fe:Sb ratio = 100 , pH 7, in Qi and Pichler, (2016)) and Sb(V) sorption on  
204 schwertmannite which was reached in 24 h (Shan *et al.*, 2023). As concentration and isotopic  
205 equilibrium time may differ (Komárek *et al.*, 2021), it was also checked that isotopic  
206 equilibrium was reached after 48 h (Table A1, Figure A3). The results showed no significant  
207 difference in Sb isotope composition between 48 h and 96 h for all conditions (Table A1,  
208 Figure A3), which confirmed isotopic equilibrium achievement at 48 h.

209 Suspensions were filtered under vacuum using a Nalgene filtration unit and 0.22  $\mu\text{m}$  pre-  
210 cleaned PVDF filters without rinsing step to avoid any bias related to Sb desorption from the  
211 mineral surfaces in line with other studies (e.g., Wasylenki *et al.*, 2015; Gueguen *et al.*, 2018;  
212 Zhou *et al.*, 2022, 2023). Air was allowed to pass through the filter for a few minutes at the  
213 end of the filtration to ensure a complete separation of the dissolved and particulate phases.  
214 The filters were dried in a vacuum desiccator. An aliquot (10 mL) of the filtrate was acidified  
215 at 1 %  $\text{HNO}_3$  for dissolved Sb and Fe concentration measurement by ICP-MS (Inductively  
216 Coupled Plasma Mass Spectrometry). Another aliquot was acidified at 1 %  $\text{HCl}$  for Sb isotope  
217 ratio analysis by HG-MC-ICP-MS (Hydride Generation Multi-Collection Inductively Coupled  
218 Plasma Mass Spectrometry). A third aliquot was either analysed the same day for redox Sb  
219 speciation or preserved in 20 mM EDTA and 87 mM acetic acid and stored at 4  $^\circ\text{C}$  until  
220 analysis (< 1 week) as this combination of acids allow to stabilise Sb(III) (Wu and Pichler,  
221 2016). The particulate phase collected on the filter was fully dissolved by placing the filter in  
222 a PTFE vial with 15 mL of 6 M  $\text{HCl}$  at 80  $^\circ\text{C}$  for 1 h (Schwertmann and Cornell, 2000) for  
223 subsequent Sb isotope analysis of the adsorbed Sb.

224 Sorption isotherms models were calculated using Freundlich and Langmuir isotherms as  
225 detailed in Appendix (Section 2, Equations A1 to A5).

## 226 2.4. Analytical methods

227 All analyses (ICP-MS, IC-ICP-MS, HG-MC-ICP-MS) were performed on the AETE-ISO  
228 platform (OSU OREME, Université de Montpellier) using routine protocols.

229 Antimony and iron concentrations in the dissolved (<0.22µm) and adsorbed (>0.22µm)  
230 fractions were measured by ICP-MS (Inductively Coupled Plasma Mass Spectrometry,  
231 iCAP TQ, ThermoScientific®) after an adequate dilution in 0.15 M HNO<sub>3</sub> (Ferrari *et al.*,  
232 2021). Dissolved Fe was below quantification limits in filtrated samples representing less than  
233 1 % of particulate Fe (except for two samples for which 4 % of total iron was in the dissolved  
234 fraction), showing that i) there was no significant dissolution of ferrihydrite or  
235 schwertmannite during the experiment and ii) colloidal ferrihydrite/schwertmannite was not  
236 present in the dissolved fraction (< 0.22 µm).

237 Antimony redox speciation analysis (Sb(V) and Sb(III) concentrations) was carried out by  
238 IC-ICP-MS (Ionic Chromatography coupled to ICP-MS, iCAP-Q, ThermoScientific®) using  
239 external Sb(III) and Sb(V) calibration. Chromatographic separation was performed using a  
240 Hamilton PRP-X100 column (15 cm x 4.6 mm i.d.) and precolumn (2 cm x 4.6 mm i.d.) with  
241 a Dionex ICS-5000 Ion Chromatography System (ThermoScientific®). A solution of 5  
242 mmol.L<sup>-1</sup> EDTA and 2 mmol.L<sup>-1</sup> KHP (pH 4.5) was used as eluent with a flow rate of  
243 1.5 mL.min<sup>-1</sup>. A solution of indium at 1 µg.L<sup>-1</sup> was continuously injected after the  
244 chromatographic separation and used as internal standard to correct potential sensitivity drifts  
245 of ICP-MS (Resongles *et al.*, 2013).

246 Antimony isotope composition was determined by HG-MC-ICP-MS (Hydride Generation  
247 coupled with a Multi-Collector ICP-MS, Neptune Plus, ThermoScientific®) as described in  
248 Ferrari *et al.*, (2021). HG-MC-ICP-MS configuration and parameters have been adapted to  
249 improve signal stability and the new settings are reported in Table A2. Antimony isotope  
250 composition was measured using a sample-standard bracketing method and is reported in the  
251 δ<sup>123</sup>Sb notation (Equation 1).

252

253 
$$\delta^{123}\text{Sb}(\text{‰}) = \left( \frac{\left(\frac{123\text{Sb}}{121\text{Sb}}\right)_{\text{sample}} - \left(\frac{123\text{Sb}}{121\text{Sb}}\right)_{\text{mean std}}}{\left(\frac{123\text{Sb}}{121\text{Sb}}\right)_{\text{mean std}}} \right) \times 1000 \text{ (Eq. 1)}$$

254 δ<sup>123</sup>Sb of the dissolved and adsorbed fractions were measured after diluting the samples to 2  
255 µg.L<sup>-1</sup> of Sb in a 3 M HCl with 0.5 % w/v KI/ascorbic acid medium to ensure a full reduction  
256 of Sb(V) to Sb(III) as required for an optimal hydride generation (Ferrari *et al.*, 2021). Each  
257 sample was measured three times, at different times in the course of analytical sessions; the  
258 results reported in Table 1 correspond to the average and standard deviation of the three  
259 measurements. The preliminary Sb purification step described in Ferrari *et al.* (2021) was not  
260 required in the present study due to the low Fe:Sb ratios (<150) and the absence of interfering

261 elements (e.g., Se, As, Te, Sn) in the experimental samples (< detection limits). Furthermore,  
262 no shift of Sb isotope composition was observed between the Sb SPEX doped in experimental  
263 matrices (0.01 M NaNO<sub>3</sub> solution or ferrihydrite/schwertmannite dissolution solution in 6 M  
264 HCl) and the pure Sb SPEX standard solution ( $\delta^{123}\text{Sb} = -0.00 \pm 0.06 \text{ ‰}$  for Sb SPEX in  
265 NaNO<sub>3</sub> solution and  $\delta^{123}\text{Sb} = -0.02 \pm 0.02 \text{ ‰}$  in Fe/HCl solution).

266  $\delta^{123}\text{Sb}$  values of the stock solutions of Sb(III) and Sb(V) used in adsorption experiments  
267 were measured (n=3) at  $0.32 \pm 0.02 \text{ ‰}$  and  $0.13 \pm 0.05 \text{ ‰}$ , respectively. Finally, different  
268 purified international certified reference materials (Sb recovery > 95 %) were measured  
269 (n=3,  $\pm 2\sigma$ ) during every analytical session to ensure the accuracy of the analysis. They  
270 included sediments GSD-3 ( $0.14 \pm 0.03 \text{ ‰}$ ), copper ore GXR-4 ( $0.39 \pm 0.01 \text{ ‰}$ ), fly ash  
271 BCR 176R ( $-0.07 \pm 0.02 \text{ ‰}$ ) and road dust BCR 723a ( $0.05 \pm 0.06 \text{ ‰}$ ) and results were  
272 within the error of published  $\delta^{123}\text{Sb}$  values (Ferrari et al., 2021). The  $\delta^{123}\text{Sb}$  estimated  
273 from the repeated measurement of the Sb SPEX solution over all analytical sessions was  
274  $0.00 \pm 0.07 \text{ ‰}$  (2SD, n=201) which is consistent with the long-term precision published for  
275 the method in Ferrari et al. (2021).

276 3. RESULTS

277 3.1. Antimony sorption behaviour

278 The complete dataset of Sb(V) and Sb(III) adsorption experiments on ferrihydrite and  
279 schwertmannite are given in Table 1 and 2, respectively. Adsorption of Sb(III) and Sb(V) on  
280 ferrihydrite and schwertmannite was better described by Freundlich rather than Langmuir  
281 isotherm models ( $0.89 < R^2 < 0.99$ , Figure A4) as previously observed for Sb(III) and Sb(V)  
282 adsorption on ferrihydrite (Qi and Pichler, 2017; Zhou et al., 2023) and Sb(V) adsorption on  
283 schwertmannite (Shan et al., 2023) suggesting that the surface sites are heterogeneous and the  
284 adsorption multi-layered. Adsorption of Sb(V) on ferrihydrite decreased from pH 6 to 8 while  
285 adsorption of Sb(III) was not affected in this pH range (except at low Fe:Sb ratio = 1), in  
286 agreement with previous studies (Guo et al., 2014; Qi and Pichler, 2017; Zhou et al., 2023).  
287 The amount of Sb(V) adsorbed on ferrihydrite (5 to 208 mg/g) was comparable to the values  
288 measured in Zhou et al. (2023) with a similar pH, Fe:Sb ratio and ferrihydrite properties. In  
289 terms of Sb surface coverage, adsorption capacity of ferrihydrite at pH 6 was similar for  
290 Sb(III) and Sb(V), with values from 23  $\mu\text{g}/\text{m}^2$  and 24  $\mu\text{g}/\text{m}^2$  for a high molar ratio Fe:Sb of  
291 127, to  $529 \pm 45 \mu\text{g}/\text{m}^2$  and  $499 \mu\text{g}/\text{m}^2$  for a low Fe:Sb ratio of 1, respectively. Adsorption of  
292 Sb(V) on schwertmannite was similar at pH 2.5 and 4.5 while adsorption of Sb(III) increased  
293 at pH 4.5 compared to pH 2.5. Schwertmannite presented a higher Sb surface coverage than  
294 ferrihydrite, for example for a Fe:Sb ratio of 1 at pH 4.5, Sb(III) and Sb(V) surface coverage  
295 were 2320 and 2289  $\mu\text{g}/\text{m}^2$ , respectively (Table 2). The sorption capacity of Sb(V) was for the  
296 lowest Fe:Sb(V) ratio at pH 2.5 was 160-205 mg/g, in the same order of magnitude of the  
297 value of 253 mg/g found by Shan et al. (2023) in similar conditions (pH=3, Fe:Sb ratio of  
298 2.5).

299 For Sb(III) adsorption experiments, dissolved Sb speciation was measured at the end of the  
300 experiments (t= 48 h). Final Sb(V) concentration was comprised between 3  $\mu\text{g}/\text{L}$  (for initial  
301 Sb concentration of 100  $\mu\text{g}/\text{L}$ ) and 197  $\mu\text{g}/\text{L}$  (for initial Sb concentrations of 10000  $\mu\text{g}/\text{L}$ )  
302 (Table 1 and 2). This was similar or even lower than initial dissolved Sb(V) concentration  
303 brought by Sb(V) contamination from the Sb(III) standard solution. Slight excess of Sb(V)  
304 was noted in ferrihydrite sorption experiments at pH 8 and high Fe:Sb ratios; however, it  
305 represented a maximum of 9 % of total initial Sb. Considering the preferential adsorption of  
306 Sb(III) over Sb(V) in competitive scenarios (Qi and Pichler, 2016, 2017), the persistence of  
307 Sb(III) as the dominant species (> 90 % after 48 h) in the dissolved fraction during Sb(III)

308 adsorption experiments suggests minimal Sb(III) oxidation. Furthermore, according to our  
309 previous experimental and theoretical investigations (Ferrari et al., 2022, 2023), abiotic  
310 Sb(III) oxidation was expected to decrease the  $\delta^{123}\text{Sb}$  value of remaining dissolved Sb(III),  
311 which was opposed to observations made in the present experiments. This is also coherent  
312 with the conclusions of Guo et al. (2014) who noted that the rapid oxidation of Sb(III) to  
313 Sb(V) due to the oxidative reactivity of Fe(III) during its adsorption is highly improbable.

**Table 1.** All experimental data of Sb(V) and Sb(III) adsorption experiments on ferrihydrite.

Samples	pH		Fe:Sb initial molar ratio	Total dissolved Sb ( $\mu\text{g/L}$ )		Dissolved Sb redox speciation ( $\mu\text{g/L}$ )			Adsorbed Sb at equilibrium (t=48 h) (%)	Surface coverage at equilibrium		Isotope composition of the dissolved fraction (t=48 h)		Isotope composition of the adsorbed fraction (t=48 h)		$\Delta^{123}\text{Sb}_{\text{solid-solution}}$ (‰)
	Average	$\sigma$		Initial (t=0 h)	Final at equilibrium (t=48 h)*	Sb(V) initial (t=0 h)**	Sb(III) final (t=48 h)***	Sb(V) final (t=48 h)***		$\mu\text{g Sb/m}^2$	mg Sb/g	$\delta^{123}\text{Sb}$ (‰) Average	$\delta^{123}\text{Sb}$ (‰) 2 $\sigma$	$\delta^{123}\text{Sb}$ (‰) Average	$\delta^{123}\text{Sb}$ (‰) 2 $\sigma$	
<b><u>Sb(V)-ferrihydrite</u></b>																
Sb(V) stock solution	n.a.	n.a.	n.a.	n.a.	n.a.	n.a.	n.a.	n.a.	n.a.	n.a.	n.a.	0.13	0.05	n.a.	n.a.	n.a.
Sb(V)_0.1ppm-pH 6	5.9	0.1	127	100	14	n.a.	n.a.	n.a.	86	23	9	0.51	0.05	0.16	0.10	-0.35
Sb(V)_0.5ppm-pH 6	6.0	0.1	25	500	130	n.a.	n.a.	n.a.	74	99	37	0.53	0.05	0.08	0.04	-0.45
Sb(V)_1ppm-pH 6	6.0	0.0	13	999	413	n.a.	n.a.	n.a.	59	158	59	0.39	0.05	-0.07	0.14	-0.46
Sb(V)_10ppm-pH 6_1	6.3	0.1	1	9990	7911	n.a.	n.a.	n.a.	21	559	208	0.26	0.06	-0.11	0.10	-0.37
Sb(V)_10ppm-pH 6_2	6.1	0.1	1	9990	8213	n.a.	n.a.	n.a.	18	478	178	0.16	0.02	-0.15	0.04	-0.31
Sb(V)_10ppm-pH 6_3	6.1	0.1	1	9990	7941	n.a.	n.a.	n.a.	21	551	205	0.10	0.11	-0.1	0.02	-0.20
Sb(V)_0.1ppm-pH 7	7.0	0.1	127	100	42	n.a.	n.a.	n.a.	58	16	6	0.39	0.02	-0.05	0.04	-0.44
Sb(V)_0.5ppm-pH 7	7.1	0.2	25	500	274	n.a.	n.a.	n.a.	45	61	23	0.28	0.06	-0.12	0.06	-0.40
Sb(V)_1ppm-pH 7	7.1	0.2	13	999	528	n.a.	n.a.	n.a.	47	127	47	0.24	0.03	-0.05	0.04	-0.29
Sb(V)_10ppm-pH 7	7.1	0.1	1	9990	8812	n.a.	n.a.	n.a.	12	317	118	0.14	0.02	-0.15	0.05	-0.29
Sb(V)_0.1ppm-pH 8	8.0	0.6	127	100	53	n.a.	n.a.	n.a.	47	13	5	0.29	0.03	0	0.09	-0.29
Sb(V)_0.5ppm-pH 8	7.9	0.6	25	500	323	n.a.	n.a.	n.a.	35	47	18	0.27	0.01	-0.11	0.10	-0.38
Sb(V)_1ppm-pH 8	8.0	0.5	13	999	585	n.a.	n.a.	n.a.	41	111	41	0.23	0.05	-0.14	0.02	-0.37
Sb(V)_10ppm-pH 8	7.9	0.5	1	9990	8440	n.a.	n.a.	n.a.	16	417	155	0.16	0.06	-0.19	0.02	-0.34
<b><u>Sb(III)-ferrihydrite</u></b>																
Sb(III) stock solution	n.a.	n.a.	n.a.	n.a.	n.a.	n.a.	n.a.	n.a.	n.a.	n.a.	n.a.	0.32	0.02	n.a.	n.a.	n.a.
Sb(III)_0.1ppm-pH 6	6.0	0.1	144	108	40	2	37	4	62	24	7	0.63	0.07	0.23	0.08	-0.40
Sb(III)_0.5ppm-pH 6	5.9	0.1	29	483	264	9	271	6	42	73	21	0.51	0.06	0.22	0.06	-0.29
Sb(III)_1ppm-pH 6	5.9	0.1	14	1072	n.d.	20	625	9	41	155	44	0.46	0.03	0.15	0.04	-0.31
Sb(III)_10ppm-pH 6	5.9	0.0	1	10626	n.d.	202	9172	48	13	499	141	0.36	0.05	0.25	0.06	-0.11
Sb(III)_0.1ppm-pH 7	7.0	0.2	144	108	n.d.	2	41	3	60	23	6	0.53	0.05	0.30	0.06	-0.24
Sb(III)_0.5ppm-pH 7	6.8	0.1	29	483	n.d.	9	206	13	54	93	26	0.51	0.05	0.24	0.03	-0.27
Sb(III)_1ppm-pH 7	6.9	0.1	14	1072	638	20	640	18	39	147	41	0.46	0.05	0.24	0.05	-0.22
Sb(III)_10ppm-pH 7	6.8	0.1	1	10626	7978	202	9267	38	12	468	132	0.38	0.08	0.07	0.05	-0.30
Sb(III)_0.1ppm-pH 8 <sup>†</sup>	8.1	0.4	144	108	n.d.	2	17	10	74	28	8	0.46	0.07	0.33	0.03	-0.13
Sb(III)_0.5ppm-pH 8	8.1	0.4	29	483	188	9	189	29	55	94	26	0.53	0.02	0.25	0.03	-0.28
Sb(III)_1ppm-pH 8	8.1	0.4	14	1072	n.d.	20	653	41	35	134	38	0.47	0.03	0.18	0.05	-0.29
Sb(III)_10ppm-pH 8	8.1	0.4	1	10626	n.d.	202	9535	130	9	341	96	0.36	0.02	0.19	0.06	-0.17

n.a. not applicable

n.d. not determined

\*Total Sb concentration determined by ICP-MS

\*\*Sb(V) concentration corresponding to 1.9% of initial Sb

\*\*\*Sb(III) and Sb(V) concentrations measured by IC-ICP-MS

<sup>†</sup>Filtration joint failure occurred during the filtration of the sample, some particles likely have been recovered in the dissolved fraction (< 0.22 $\mu\text{m}$ ).

**Table 2.** All experimental data of Sb(V) and Sb(III) adsorption experiments on schwertmannite.

Samples	pH		Fe:Sb initial molar ratio	Total dissolved Sb ( $\mu\text{g/L}$ )		Dissolved Sb redox speciation ( $\mu\text{g/L}$ )			Adsorbed Sb at equilibrium (t=48 h) (%)	Surface coverage at equilibrium		Isotope composition of the dissolved fraction (t=48 h)		Isotope composition of the adsorbed fraction (t=48 h)		$\Delta^{123}\text{Sb}_{\text{solid-}}^{\text{solution}}$ (%)
	Average	$\sigma$		Initial (t=0 h)	Final at equilibrium (t=48 h)*	Sb(V) initial (t=0 h)**	Sb(III) final (t=48 h)***	Sb(V) final (t=48 h)***		$\mu\text{g Sb/m}^2$	mg Sb/g	$\delta^{123}\text{Sb}$ (‰) Average	$\delta^{123}\text{Sb}$ (‰) 2 $\sigma$	$\delta^{123}\text{Sb}$ (‰) Average	$\delta^{123}\text{Sb}$ (‰) 2 $\sigma$	
<b><u>Sb(V)-schwertmannite</u></b>																
Sb(V)_0.1ppm-pH 2.5	2.6	0.0	120	112	26	n.a.	n.a.	n.a.	76	171	9	0.35	0.02	0.07	0.03	-0.28
Sb(V)_0.5ppm-pH 2.5	2.6	0.0	24	475	210	n.a.	n.a.	n.a.	56	529	26	0.31	0.04	0.01	0.05	-0.30
Sb(V)_1ppm-pH 2.5	2.6	0.2	12	1179	451	n.a.	n.a.	n.a.	62	1455	73	0.29	0.07	-0.01	0.09	-0.30
Sb(V)_10ppm-pH 2.5_1	2.6	0.0	1.2	9990	8393	n.a.	n.a.	n.a.	16	3195	160	0.16	0.02	-0.10	0.07	-0.26
Sb(V)_10ppm-pH 2.5_2	2.6	0.1	1	9990	7936	n.a.	n.a.	n.a.	21	4110	205	0.15	0.04	-0.08	0.06	-0.23
Sb(V)_0.1ppm-pH 4.5	4.6	0.0	120	112	6	n.a.	n.a.	n.a.	95	212	11	0.42	0.04	0.13	0.06	-0.29
Sb(V)_0.5ppm-pH 4.5	4.6	0.0	24	475	106	n.a.	n.a.	n.a.	78	738	37	0.43	0.03	0.11	0.07	-0.31
Sb(V)_1ppm-pH 4.5	4.6	0.0	12	1179	410	n.a.	n.a.	n.a.	65	1537	77	0.31	0.04	0.03	0.06	-0.28
Sb(V)_10ppm-pH 4.5_1	4.6	0.1	1	9990	8831	n.a.	n.a.	n.a.	12	2320	116	0.17	0.03	-0.05	0.07	-0.21
Sb(V)_10ppm-pH 4.5_2	4.6	0.1	1	9990	9544	n.a.	n.a.	n.a.	4	894	45	0.17	0.02	-0.06	0.02	-0.23
<b><u>Sb(III)-schwertmannite</u></b>																
Sb(III)_0.1ppm-pH 2.5	2.6	0.0	120	107	38	2	28	2	65	140	7	0.66	0.04	0.20	0.05	-0.46
Sb(III)_0.5ppm-pH 2.5	2.6	0.1	24	527	254	10	202	7	52	546	27	0.53	0.02	0.14	0.03	-0.39
Sb(III)_1ppm-pH 2.5	2.6	0.1	12	1058	708	20	630	15	33	699	35	0.48	0.04	0.09	0.05	-0.39
Sb(III)_10ppm-pH 2.5	2.6	0.1	1	9991	9281	190	9204	178	7	1421	71	0.34	0.03	0.02	0.07	-0.32
Sb(III)_0.1ppm-pH 4.5	4.6	0.0	120	107	12	2	7	3	89	190	10	0.68	0.01	0.35	0.05	-0.33
Sb(III)_0.5ppm-pH 4.5	4.5	0.0	24	527	114	10	108	4	78	826	41	0.62	0.08	0.28	0.03	-0.34
Sb(III)_1ppm-pH 4.5	4.5	0.1	12	1058	385	20	341	32	64	1345	67	0.59	0.06	0.22	0.06	-0.37
Sb(III)_10ppm-pH 4.5	4.4	0.1	1	9991	8846	190	8478	197	11	2289	114	0.38	0.07	0.12	0.04	-0.26

n.a. not applicable

n.d. not determined

\*Total Sb concentration determined by ICP-MS

\*\*Sb(V) concentration corresponding to 1.9% of initial Sb

\*\*\*Sb(III) and Sb(V) concentrations measured by IC-ICP-MS

316

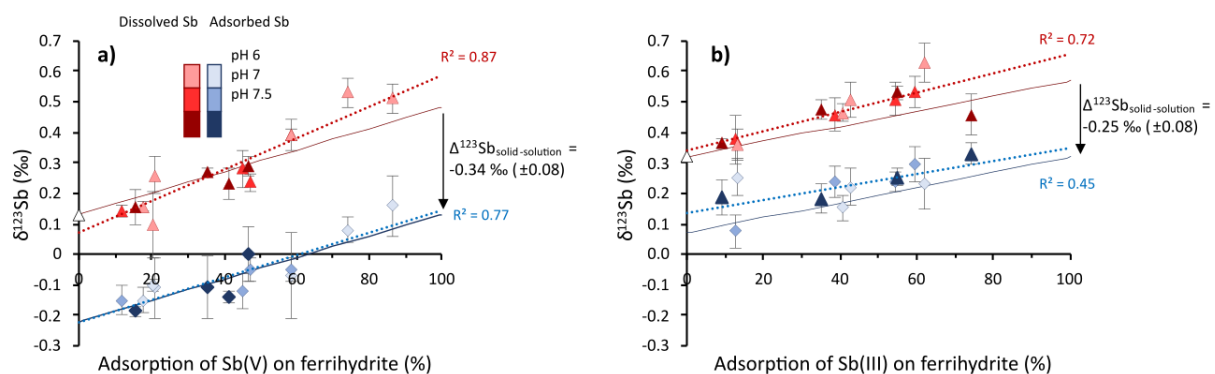
## 3.2. Antimony isotope fractionation

317

## 3.2.1 Isotope fractionation during Sb adsorption on ferrihydrite

318

319 There was a significant isotope fractionation of Sb between the dissolved and adsorbed  
 320 phases. The isotope fractionation during adsorption of Sb(V) and Sb(III) on ferrihydrite  
 321 followed a closed-system equilibrium fractionation model ( $R^2 = 0.87$  for dissolved Sb(V)  
 322 experimental vs modelled values and  $R^2 = 0.64$  for Sb(III), Figure A5), with a parallel increase  
 323 of the isotopic signature of the dissolved and adsorbed phases (Figure 1). The fractionation  
 324 factor  $\Delta^{123}\text{Sb}_{\text{solid-solution}}$  averaged  $-0.34 \pm 0.08$  ‰ for Sb(V) and  $-0.25 \pm 0.08$  ‰ for Sb(III),  
 325 with the dissolved phase preferentially enriched in the heavy isotope ( $^{123}\text{Sb}$ ), for both Sb(III)  
 326 and Sb(V) species. Under the experimental conditions, pH and Sb surface coverage did not  
 327 influence the magnitude of  $\Delta^{123}\text{Sb}_{\text{solid-solution}}$  fractionation factor (Figure 2a-c). Only one data  
 328 point from Sb(III) sorption experiments deviated from the general trend for the dissolved phase in  
 329 Figure 1b; it was the sample with 74 % adsorption at pH 8, for which a failure of the filter  
 330 joint occurred during the filtration most likely causing the release of some particles into the  
 dissolved fraction and explaining the lower  $\Delta^{123}\text{Sb}_{\text{solid-solution}}$  observed (this is also supported



331 by the presence of 4 % of initial solid Fe in solution at equilibrium).

332 **Figure 1.** Antimony isotope composition ( $\delta^{123}\text{Sb}$ ) of dissolved (red) and adsorbed (blue)  
 333 phases during (a) Sb(V) and (b) Sb(III) adsorption on ferrihydrite. The white triangles  
 334 represent the signature of starting Sb(III) or Sb(V) stock solutions. Dotted lines represent the  
 335 regression lines for the entire dissolved (red) or adsorbed (blue) experimental dataset. Solid  
 336 lines represent the theoretical  $\delta^{123}\text{Sb}$  of the dissolved (red) and adsorbed (blue) Sb using an  
 337 equilibrium fractionation model and the average  $\Delta^{123}\text{Sb}_{\text{solid-solution}}$  determined experimentally.



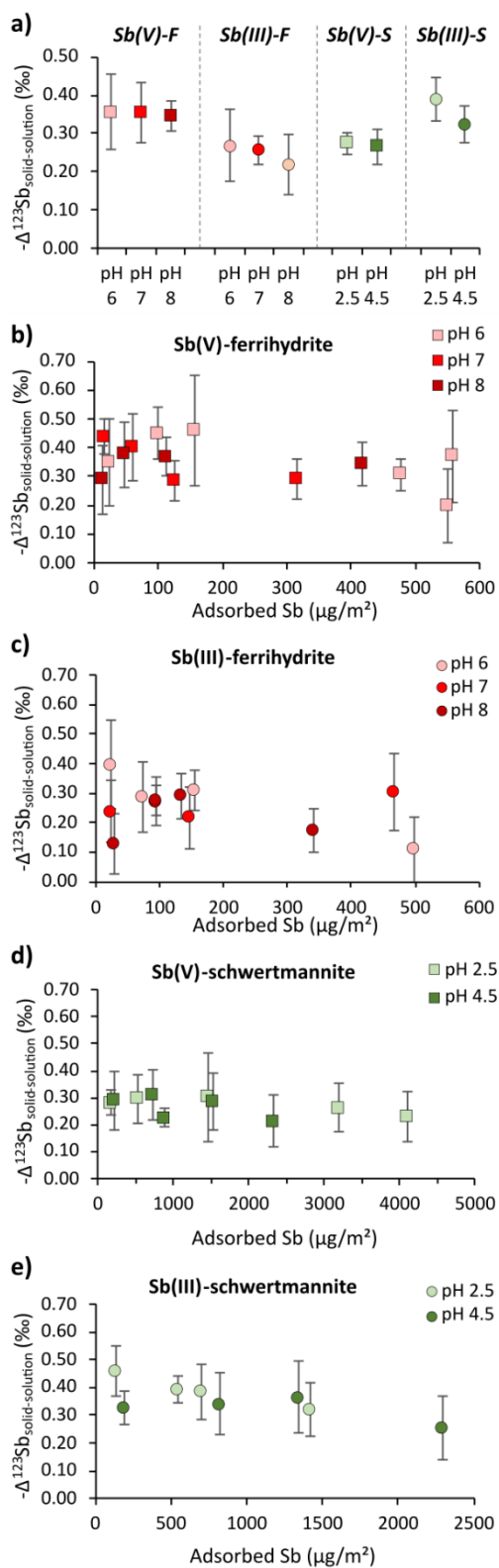


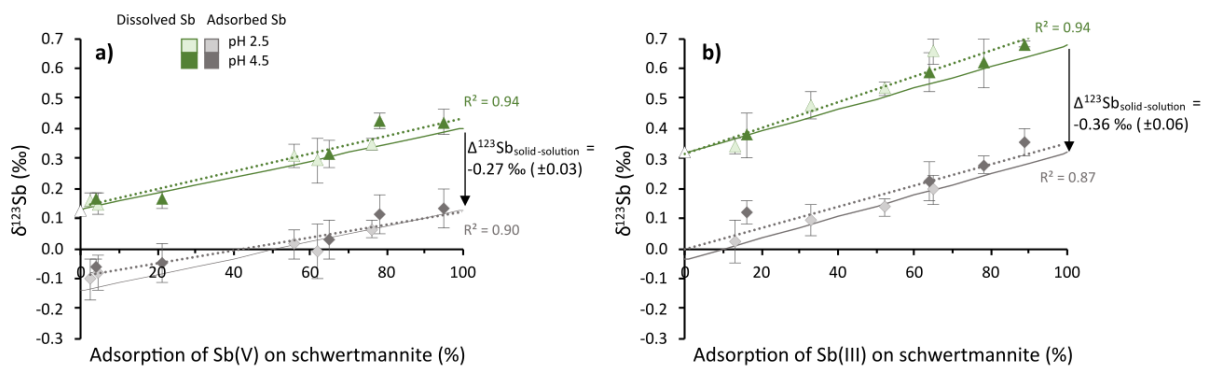
**Figure 2.** a) Average apparent fractionation factor between the solution and the solid phase ( $-\Delta^{123}\text{Sb}_{\text{solid-solution}}$ ) calculated at pH 6, 7 and 8 for Sb(V) (*Sb(V)-F*) and Sb(III) (*Sb(III)-F*) adsorption on ferrihydrite and at pH 2.5 and 4.5 for Sb(V) (*Sb(V)-S*) and Sb(III) (*Sb(III)-S*) adsorption on schwertmannite. Figures 2b to 2e represent the average apparent fractionation factor ( $-\Delta^{123}\text{Sb}_{\text{solid-solution}}$ ) as a function of Sb surface coverage ( $\mu\text{g}/\text{m}^2$ ) during adsorption of b) Sb(V) on ferrihydrite, c) Sb(III) on ferrihydrite, d) Sb(V) on schwertmannite and e) Sb(III) on schwertmannite. On Figures 2b to 2e, the error bars correspond to the propagation of the analytical error on the measurement of dissolved and adsorbed isotopic composition ( $\delta^{123}\text{Sb}$ ).

354

### 3.2.2 Isotope fractionation during Sb adsorption on schwertmannite

355 The fractionation of  $\delta^{123}\text{Sb}$  was also significant between the dissolved and adsorbed phases  
356 during Sb adsorption on schwertmannite. As for the adsorption of Sb species on ferrihydrite,  
357 the adsorption of Sb(V) and Sb(III) on schwertmannite followed a closed system equilibrium  
358 fractionation model (Figure 3, Figure A5 :  $R^2 = 0.94$  for dissolved Sb(V) and Sb(III) between  
359 modelled and experimental data). The fractionation factor  $\Delta^{123}\text{Sb}_{\text{solid-solution}}$  averaged  $-0.36 \pm$   
360  $0.06 \text{ ‰}$  for Sb(III) and  $-0.27 \pm 0.03 \text{ ‰}$  for Sb(V), with the dissolved phase preferentially  
361 enriched in the heavy isotope ( $^{123}\text{Sb}$ ). Neither the pH nor the surface coverage significantly  
362 influenced Sb isotope fractionation within the range experimental conditions (Figure 2a, d and  
363 e).

364



365

366 **Figure 3.** Antimony isotope composition ( $\delta^{123}\text{Sb}$ ) of dissolved (green) and adsorbed (grey)  
367 phases during (a) Sb(V) and (b) Sb(III) adsorption on schwertmannite. The white triangles  
368 represent the signature of starting Sb(III) or Sb(V) stock solutions. Dotted lines represent the  
369 regression lines for the entire dissolved (green) or adsorbed (grey) experimental dataset. Solid  
370 lines represent the theoretical  $\delta^{123}\text{Sb}$  of the dissolved (green) and adsorbed (grey) Sb using an  
371 equilibrium fractionation model and the average  $\Delta^{123}\text{Sb}_{\text{solid-solution}}$  determined experimentally.

372

## 373 4. DISCUSSION

### 374 4.1. Antimony isotope fractionation during its adsorption of ferrihydrite

375 Only a few other studies investigated the fractionation of antimony isotopes on iron- (Araki  
376 et al., 2009; Zhou et al., 2023) or aluminium- (Zhou *et al.*, 2022) oxyhydroxides and these  
377 studies focused only on the sorption of Sb(V) species. Zhou *et al.* (2022) showed that  
378 although kinetic fractionation occurs at the early stage of the reaction, Sb(V) adsorption on  
379 aluminium oxides does not produce significant equilibrium Sb isotope fractionation and  
380 explained the lack of fractionation by the formation of an outer-sphere complex of Sb on  $\gamma$ -  
381  $\text{Al}_2\text{O}_3$ , with similar bond length of Sb - O ( $\sim 1.98 \text{ \AA}$ ) and octahedral bond structure of  
382  $\text{Sb}(\text{OH})_6^-$  in the aqueous and solid phases (Zhou et al., 2022). On the other hand, our study  
383 shows a preferential adsorption of the light  $^{121}\text{Sb}(\text{III})$  and  $^{121}\text{Sb}(\text{V})$  isotope onto ferrihydrite  
384 and schwertmannite, with a fractionation factor  $\Delta^{123}\text{Sb}_{\text{solid-solution}}$  around -0.3 ‰. This value is  
385 similar, yet slightly lower, to the equilibrium fractionation factor ( $\Delta^{123}\text{Sb}_{\text{solid-solution}}$  of -0.49  
386 ‰) measured by Zhou et al. (2023) for Sb(V) adsorption on ferrihydrite while antimony(V)  
387 adsorption on hematite and goethite generated higher fractionation ( $\Delta^{123}\text{Sb}_{\text{solid-solution}} = -1.12 \pm$   
388  $0.01 \text{ ‰}$  for hematite and  $-1.14 \pm 0.05 \text{ ‰}$  for goethite).

389 For the sorption of Sb(V) on ferrihydrite, sorption mechanisms and local structures of  
390 adsorbed-Sb(V) can be obtained from previous sorption studies carried out in similar  
391 conditions. In the study of Araki *et al.* (2009) and Zhou et al. (2023) which both evidenced  
392 slight enrichment in the heavy isotope in the aqueous phase compared to Sb(V) adsorbed on  
393 ferrihydrite, Sb(V) was present as an inner-sphere complex of octahedral Sb species on the  
394 ferrihydrite surface (Mitsunobu *et al.*, 2006; Zhou et al., 2023). Thus, the octahedral bond  
395 structure of Sb(V) was the same in the aqueous ( $\text{Sb}(\text{OH})_6^-$ ) and adsorbed Sb(V). There was no  
396 change in the first coordination shell between aqueous and adsorbed Sb(V) both in terms of  
397 coordination number and Sb(V)-O bond lengths of  $\sim 1.97\text{-}1.98 \text{ \AA}$  (Mitsunobu et al., 2010;  
398 Tella and Pokrovsky, 2012; Zhou et al., 2023). The sorption process involved the formation of  
399 Sb - O - Fe bonds with an edge-sharing and corner-sharing configurations (Scheinost *et al.*,  
400 2006; McComb *et al.*, 2007, Guo et al., 2014). This was confirmed by Mitsunobu *et al.* (2010)  
401 who also demonstrated the double corner-sharing complex character of the inner-sphere  
402 formation and more recently by Zhou et al. (2023). One could have expected that this mode of  
403 complexation would generate no fractionation or slight enrichment in the heavy isotope in the  
404 adsorbed Sb(V) species (stronger bonding due to inner-sphere complexation), while the

405 reverse was observed. Nickel adsorption onto various Fe oxyhydroxides through inner-sphere  
406 complexes also showed lighter Ni isotope enrichment in the adsorbed fraction on ferrihydrite  
407 ( $\Delta^{60/58}\text{Ni}_{\text{solid-solution}}$  value of  $-0.35 \pm 0.10$  ‰ for Ni on ferrihydrite, (Wasylenki *et al.*, 2015;  
408 Wang and Wasylenki, 2017; Gueguen *et al.*, 2018)). Considering that Ni - O bonds in the  
409 adsorbed complexes were not significantly longer and weaker (therefore, Ni bonding was not  
410 weaker) than in the predominant aqueous species, the authors ascribed this fractionation  
411 direction to distortions of bond angles and lengths occurring in the adsorbed complexes  $\text{NiO}_6$   
412 (Wasylenki *et al.*, 2015). More recently, Yan *et al.* (2021) observed the same effect for Cd;  
413 fractionation of Cd isotopes during sorption onto Fe oxyhydroxides and enrichment in the  
414 light isotopes in the solid were attributed to distortion of the  $\text{CdO}_6$  complexes during  
415 adsorption (Yan *et al.*, 2021). For antimony, our theoretical calculations using the Density  
416 Functional Theory suggested that the appearance in the structure of a second neighbour other  
417 than the Sb species induced a slight distortion of the atomic polyhedron (both on Sb - O bond  
418 lengths and on the O - Sb - O angle) susceptible to cause isotopic fractionation of around 0.3  
419 ‰, in the same order of magnitude as measured in this study (Ferrari *et al.*, 2022). In the  
420 present study, the atomic distortion induced by iron as the second closest neighbour may be  
421 the cause of the slight enrichment in lighter Sb isotopes in the solid. Regarding the possible  
422 effect of surface coverage on the isotope fractionation during sorption (evidenced for example  
423 for Zn adsorption onto Mn oxyhydroxide, Bryan *et al.*, 2015), our data showed no influence,  
424 within a range of Fe:Sb molar ratios of 1.4 - 144 (Sb(III)) and 1.3 - 126 (Sb(V)). This was in  
425 agreement with the results of Mitsunobu *et al.* (2010) and Zhou *et al.* (2023) who showed that  
426 there was no change in the local structures of Sb species in Sb(V)-adsorbed ferrihydrite at  
427 various Fe:Sb ratios (20-1000).

428 pH has an important effect on the sorption of metals and metalloids onto Fe-oxyhydroxides  
429 because it influences both the surface charge of the solid (thus, the surface coverage) and the  
430 aqueous speciation of elements (thus the potential fractionation among the aqueous species  
431 and the possible different affinity of the different aqueous species for the solid). Therefore, pH  
432 changes may induce variations in metal isotope fractionation factors between adsorbed and  
433 aqueous species (for example for Zn, see references in Komárek *et al.* (2021); for Mo  
434 (Goldberg *et al.*, 2009) ; or for Se (Xu *et al.*, 2020)). Here, Sb(V) sorption on ferrihydrite was  
435 higher at pH 6 than at pH 7 - 8. The point of zero charge (pzc) of synthetic Fe-oxides usually  
436 ranges between pH 7 and 9 (Parks, 1965; Schwertmann and Cornell, 2000), which suggests  
437 that the surface charge of ferrihydrite in the present sorption experiments could be slightly  
438 more positive at pH 6 than at pH 7 - 8. Regarding Sb speciation in solution, Sb(V) species

439 belongs to the acid/base couple  $\text{Sb}(\text{OH})_5/\text{Sb}(\text{OH})_6^-$ , with a pKa value of 2.848 (25 °C)  
440 (Accornero *et al.*, 2008); thus, Sb(V) is in the form of anionic  $\text{Sb}(\text{OH})_6^-$  species in the whole  
441 pH range of sorption experiments on ferrihydrite (pH 6 – 8) (Filella *et al.*, 2002). Therefore,  
442 the higher Sb(V) sorption on ferrihydrite at pH 6 could be related to the slight change of  
443 ferrihydrite surface charge. However, this change did not significantly affect Sb isotope  
444 fractionation amplitude. A similar result was obtained for selenium; although pH influenced  
445 the amount of Se(IV) adsorbed on hematite, it did not significantly change Se isotopic  
446 fractionation (Xu *et al.*, 2020) and for Sb(V) adsorbed on ferrihydrite, hematite and goethite  
447 which did not show changes in complex structures with varying pH (Zhou *et al.*, 2023).

448 Regarding Sb(III), aqueous speciation was not expected to change significantly over the  
449 whole pH range of ferrihydrite sorption experiments (6 – 8) (representing either 100% of  
450 uncharged  $\text{Sb}(\text{OH})_3$  over pH 6 – 8 (Filella *et al.*, 2002) or > 85 % of anionic tartrate complex  
451 over pH 6 – 8 (Biver, 2021), depending if tartrate complexation is considered or not). This is  
452 consistent with the negligible effect of pH on sorption isotherms and Sb isotope fractionation  
453 between adsorbed and aqueous Sb observed in the present study. Antimony isotope  
454 fractionation resulting from the adsorption of Sb(III) on ferrihydrite was on average slightly  
455 lower than that of Sb(V) possibly due to slight differences in complexation configuration as  
456 observed among the different mineral phases (Zhou *et al.*, 2022, 2023) but the difference  
457 remains small and would require an in-depth molecular speciation study to be further  
458 discussed.

#### 459 4.2. Influence of the mineral nature

460 Metal isotope fractionation during their adsorption on minerals varies according to the  
461 mineralogy (Komárek *et al.*, 2021). Here, sorption experiments with schwertmannite were  
462 conducted at acid pH values (i.e., 2.5 – 4.5), corresponding to the stability domain of this  
463 mineral, which is different from that of ferrihydrite (i.e., 6 – 8); thus, the effects of mineral on  
464 Sb isotope fractionation during sorption cannot be distinguished from pH effect. Sorption  
465 studies of antimony on schwertmannite are rare in the literature. Nagano *et al.* (2011) showed  
466 that Sb oxyanions had a high affinity for natural schwertmannite found in AMD-impacted  
467 river and suggested the formation of inner-sphere complexes at the schwertmannite surface.  
468 Shan *et al.* (2023) recently revealed that Sb(V) is complexed on schwertmannite through the  
469 formation of edge-sharing and double corner-sharing complexes at the surface and the tunnel  
470 inner-surface of schwertmannite similarly to ferrihydrite. The proportion of surface species

471 was dependent on pH (in the pH range 3-9) and on Sb loading (in the Fe:Sb ratio range 2.5 –  
472 250); at low Sb(V) loading and alkaline pH, Sb(V) sorption was also accompanied by the  
473 incorporation of Sb(V) in the mineral lattice (Shan et al. 2023). In the present study, Sb  
474 isotope fractionation was not significantly different between pH 2.5 and 4.5 probably because  
475 the proportion of Sb(V) surface species does not vary significantly in this pH range, in  
476 agreement with the surface complexation modelling calculations of Shan et al. (2023). The Sb  
477 surface coverage (Fe:Sb from 1.2 to 120) did not influence Sb isotope fractionation suggesting  
478 that Sb(V) incorporation in the Fe-O octahedron does not fractionate Sb isotopes or that the  
479 proportion of Sb(V) incorporated remains too limited to affect the apparent isotope  
480 fractionation.

481 Only one study, Li *et al.* (2016), investigated the sorption behaviour of Sb(III) and Sb(V) on  
482 schwertmannite separately, at different pH. Over the pH range 3.5 - 5.0, Sb(III) and Sb(V) are  
483 adsorbed efficiently (Li *et al.*, 2016). Our results corroborated these findings, with very  
484 similar maximum Sb sorption densities obtained for Sb(III) (2289  $\mu\text{g}\cdot\text{m}^2$ , i.e., 114  $\text{mg}\cdot\text{g}^{-1}$ ) and  
485 for Sb(V) (2320  $\mu\text{g}\cdot\text{m}^2$ , i.e., 116  $\text{mg}\cdot\text{g}^{-1}$ ) at pH 4.5. pH had little effect on the sorption of  
486 Sb(V) on schwertmannite (Sb(OH)<sub>6</sub><sup>-</sup> predominated over Sb(OH)<sub>5</sub> at pH 2.5 and 4.5 (Filella et  
487 al., 2002)) while Sb(III) sorption increased slightly at pH 4.5 compared to pH 2.5, which  
488 could be related to change in schwertmannite protonation (Li et al., 2016) rather than change  
489 in aqueous Sb(III) speciation (predominant Sb(III) species did not change at pH 2.5 and at pH  
490 4.5, whether tartrate complexation is considered (Biver, 2021) or not (Filella et al., 2002) in  
491 the speciation calculation). Nevertheless, the slight change of reactivity of Sb(III) with pH had  
492 no significant effect on Sb isotope fractionation between adsorbed- and aqueous-Sb, and  
493 finally the amplitude and direction of Sb isotope fractionation factors with schwertmannite  
494 were similar to those obtained with ferrihydrite. In both cases, the isotope fractionation could  
495 arise from the distortion of the atomic polyhedron of Sb(III) and Sb(V) during sorption and  
496 the apparition of Fe-Sb in the second shell, which leads to small changes in bond lengths,  
497 angles and volume, and induces an increase of the disorder of the structure and thus weaker  
498 bonds favouring light isotopes. Such a mechanism has been suggested to explain isotope  
499 fractionation observed in several sorption studies for Ge (Pokrovsky *et al.*, 2014), Mo  
500 (Wasylenki *et al.*, 2011), Cd (Yan *et al.*, 2021) and Ni (Wasylenki *et al.*, 2015; Wang and  
501 Wasylenki, 2017; Gueguen *et al.*, 2018), and theoretical study for Sb (Ferrari *et al.*, 2022).  
502 Extended X-ray adsorption fine structure (EXAFS) measurements would be necessary to  
503 better characterise the local structure of Sb(III) species in ferrihydrite and schwertmannite.

504

### 4.3. Environmental significance

505 Schwertmannite and ferrihydrite are typical Sb-bearing phases in rivers impacted by AMD  
506 and the main control of Sb mobility. The experimental conditions (mineral phases, pH, initial  
507 concentration of Sb(V) and Sb(III), ionic strength) were designed to be relevant to natural  
508 waters impacted by AMD. Therefore, the relatively uniform fractionation factor  $\Delta^{123}\text{Sb}_{\text{solid-}}$   
509  $\text{solution}$  around -0.3 ‰ obtained between adsorbed- and aqueous-Sb in the present study is of  
510 particular interest in the perspective of tracing sorption process in environmental studies.  
511 However, this value obtained in laboratory conditions with simple solution chemistry must be  
512 compared to apparent fractionation factors in real AMD-impacted streams whose chemistry is  
513 more complex than experimental conditions. A few data are available from the literature; a  
514 slight heavy Sb isotopic enrichment was observed in a drainage water sample from the  
515 Ichinokawa mine in Japan compared to the data from Sb minerals ( $\text{Sb}_2\text{S}_3$ ) collected in the  
516 same area (Tanimizu *et al.*, 2011). The isotopic fractionation was ascribed to adsorption  
517 equilibrium with Fe hydroxides in the surrounding sediment. It was in line with the results of  
518 laboratory experiments of Sb(V) sorption on ferrihydrite which also indicated a slight  
519 enrichment of the heavier Sb isotope in the aqueous phase compared to adsorbed Sb (Araki *et*  
520 *al.*, 2009). In an ongoing study, Resongles *et al.* (2021) showed an apparent fractionation of -  
521 0.35‰ between river sediments and water in a stream impacted by AMD at the San José mine  
522 (Oruro, Bolivia), suggesting that adsorption may be an important process leading to an  
523 enrichment in heavy Sb isotope in AMD waters. These results tend to validate the  
524 fractionation factors obtained in the laboratory in the present study and show that Sb isotopes  
525 may be useful to investigate the mechanisms controlling Sb fate in mining-impacted rivers.  
526 However, recent studies also showed that biotic and abiotic redox changes generate Sb isotope  
527 fractionation with factors in the same order of magnitude as observed for adsorption  
528 indicating that Sb isotope signature in natural systems can result from a complex series of  
529 processes (Ferrari *et al.*, 2023, Veldhuizen *et al.*, 2023). Besides, molecular-scale studies  
530 showed that the incorporation of Sb(V) into the structure of schwertmannite by substitution of  
531 Fe(III) occurs at low Sb(V) loading and alkaline pH, stabilizing the schwertmannite over a  
532 larger range of pH (Rastegari *et al.*, 2022, Shan *et al.*, 2023), further study of the isotope  
533 fractionation associated with this process would be required.

534

535 5. CONCLUSION

536

537 This study showed that sorption on ferrihydrite and schwertmannite induced a slight  
538 enrichment in the light isotopes in adsorbed Sb, with no significant effect of pH, Fe:Sb ratio,  
539 or redox Sb species under the study conditions. The  $\Delta^{123}\text{Sb}_{\text{solid-solution}}$  values obtained for  
540 sorption on ferrihydrite were  $-0.25 \pm 0.08 \text{ ‰}$  for Sb(III) and  $-0.34 \pm 0.08 \text{ ‰}$  for Sb(V). For  
541 sorption on schwertmannite, the  $\Delta^{123}\text{Sb}_{\text{solid-solution}}$  values obtained were  $-0.36 \pm 0.06 \text{ ‰}$  for  
542 Sb(III) and  $-0.27 \pm 0.03 \text{ ‰}$  for Sb(V). The observed isotopic fractionation followed a closed  
543 system equilibrium model and could result from the distortion of the atomic polyhedron  
544 formed by Sb(III) and Sb(V) due to the appearance of iron as second closest Sb neighbour  
545 during the Sb adsorption, thus decreasing the polyhedral symmetry. This study gives new  
546 interpretation tools for the understanding of the isotopic cycle of Sb in mining and natural  
547 environments.

548

## 549 6. ACKNOWLEDGEMENTS

550 This work received financial support from the CNRS INSU EC2CO program (Project  
551 AntiBol), the French Research National Agency ANR (project ANTIMONY, grant number  
552 ANR-22-CE01-0016-01) and the Ecole Doctorale GAIA (PhD fellowship of Colin Ferrari,  
553 2019-2022). We thank Sophie Delpoux and Léa Causse for the speciation and trace element  
554 analysis performed on the AETE-ISO platform, OSU OREME/Université de Montpellier and  
555 Laura Blanc, David Clousier and Léa Pradeilles for their help during the experiments. We  
556 would like to acknowledge Nicolas Donzel and Bernard Fraisse from the PAC platform and  
557 Frédéric Hernandez from the MEA platform, Université de Montpellier, for BET surface area  
558 measurement, DRX analysis and SEM images, respectively.

559



- 561 Accornero, M., Marini, L. and Lelli, M. (2008) ‘The Dissociation Constant of Antimonic Acid  
562 at 10–40 °C’, *Journal of Solution Chemistry*, 37(6), pp. 785–800.  
563 <https://doi.org/10.1007/s10953-008-9280-4>.
- 564 Araki, Y., Tanimizu, M. and Takahashi, Y. (2009) ‘Antimony isotopic fractionation during  
565 adsorption on ferrihydrite’, *Geochimica et Cosmochimica Acta Supplement*, 73, p. A49.
- 566 Asaoka, S. *et al.* (2011) ‘Preconcentration Method of Antimony Using Modified Thiol Cotton  
567 Fiber for Isotopic Analyses of Antimony in Natural Samples’, *Analytical Sciences*, 27, pp.  
568 25–28. <https://doi.org/10.2116/analsci.27.25>
- 569 Balistrieri, L.S. *et al.* (2008) ‘Fractionation of Cu and Zn isotopes during adsorption onto  
570 amorphous Fe(III) oxyhydroxide: Experimental mixing of acid rock drainage and ambient  
571 river water’, *Geochimica et Cosmochimica Acta*, 72(2), pp. 311–328.  
572 <https://doi.org/10.1016/j.gca.2007.11.013>.
- 573 Beauchemin, S. *et al.* (2012). Downstream changes in antimony and arsenic speciation in  
574 sediments at a mesothermal gold deposit in British Columbia, Canada. *Applied geochemistry*,  
575 27(10), pp. 1953-1965. <https://doi.org/10.1016/j.apgeochem.2012.04.003>.
- 576 Belzile, N., Chen, Y.-W. and Wang, Z. (2001) ‘Oxidation of antimony (III) by amorphous  
577 iron and manganese oxyhydroxides’, *Chemical Geology*, 174(4), pp. 379–387.  
578 [https://doi.org/10.1016/S0009-2541\(00\)00287-4](https://doi.org/10.1016/S0009-2541(00)00287-4).
- 579 Bolan, N., *et al.* (2022) ‘Antimony contamination and its risk management in complex  
580 environmental settings: a review.’ *Environment International*, 158, pp. 106908.  
581 <https://doi.org/10.1016/j.envint.2021.106908>
- 582 Kaufmann, B. *et al.* (2021) ‘In-situ determination of antimony isotope ratios in Sb minerals by  
583 femtosecond LA-MC-ICP-MS’, *Journal of Analytical Atomic Spectrometry*, 36, pp. 1554-  
584 1567. <https://doi.org/10.1039/D1JA00089F>.
- 585 Bigham, J.M. *et al.* (1996) ‘Schwertmannite and the chemical modeling of iron in acid sulfate  
586 waters’, *Geochimica et Cosmochimica Acta*, 60(12), pp. 2111–2121.  
587 [https://doi.org/10.1016/0016-7037\(96\)00091-9](https://doi.org/10.1016/0016-7037(96)00091-9).
- 588 Biver, M., and Shotyk, W. (2012) ‘Experimental study of the kinetics of ligand-promoted  
589 dissolution of stibnite (Sb<sub>2</sub>S<sub>3</sub>)’, *Chemical Geology*, 294, pp. 165–172.  
590 <https://doi.org/10.1016/j.chemgeo.2011.11.009>.
- 591 Biver, M. (2021) ‘A Comprehensive Potentiometric Study of the Tartrate Complexes of  
592 Trivalent Arsenic, Antimony, and Bismuth in Aqueous Solution’, *Inorganic Chemistry*,  
593 60(23), pp. 18360–18369. <https://doi.org/10.1021/acs.inorgchem.1c02962>.
- 594 Bryan, A.L. *et al.* (2015) ‘Zinc isotope fractionation during adsorption onto Mn oxyhydroxide  
595 at low and high ionic strength’, *Geochimica et Cosmochimica Acta*, 157, pp. 182–197.  
596 <https://doi.org/10.1016/j.gca.2015.01.026>.

597 European Commission (2020) ‘*Communication From The Commission To The European*  
598 *Parliament, The Council, The European Economic And Social Committee And The Committee*  
599 *Of The Regions. Critical Raw Materials Resilience: Charting a Path towards greater Security*  
600 *and Sustainability*’, Communication COM(2020)474.

601 Degryse, P. *et al.* (2015) ‘Isotopic investigation into the raw materials of Late Bronze Age  
602 glass making’, *Journal of Archaeological Science*, 62, pp. 153–160.  
603 <https://doi.org/10.1016/j.jas.2015.08.004>.

604 Degryse, P. *et al.* (2020) ‘Isotopic evidence for the use of Caucasian antimony in Late Bronze  
605 Age glass making’, *Journal of Archaeological Science*, 120, p. 105195.  
606 <https://doi.org/10.1016/j.jas.2020.105195>.

607 Essington, M.E. and Stewart, M.A. (2018) ‘Adsorption of Antimonate, Sulfate, and Phosphate  
608 by Goethite: Reversibility and Competitive Effects’, *Soil Science Society of America Journal*,  
609 82(4), pp. 803–814. <https://doi.org/10.2136/sssaj2018.01.0003>.

610 Ferrari, C. *et al.* (2021) ‘Correction for: A single-step purification method for the precise  
611 determination of antimony isotopic composition of environmental, geological and biological  
612 samples by HG-MC-ICP-MS’, *Journal of Analytical Atomic Spectrometry*, 36(4), pp. 776–  
613 785. <https://doi.org/10.1039/D1JA90048J>

614 Ferrari, C. *et al.* (2022) ‘Equilibrium mass-dependent isotope fractionation of antimony  
615 between stibnite and Sb secondary minerals: A first-principles study’, *Chemical Geology*,  
616 611, p. 121115. <https://doi.org/10.1016/j.chemgeo.2022.121115>.

617 Ferrari, C., *et al.* (2023) ‘Antimony isotopic fractionation during Sb (III) oxidation to Sb (V):  
618 Biotic and abiotic processes.’ *Chemical Geology* 641 (2023): 121788.  
619 <https://doi.org/10.1016/j.chemgeo.2023.121788>.

620 Filella, M., Belzile, N. and Chen, Y.-W. (2002) ‘Antimony in the environment: a review  
621 focused on natural waters: I. Occurrence’, *Earth-Science Reviews*, 57, pp. 125–176.  
622 [https://doi.org/10.1016/S0012-8252\(01\)00070-8](https://doi.org/10.1016/S0012-8252(01)00070-8).

623 Filella, M., Williams, P.A. and Belzile, N. (2009) ‘Antimony in the environment : knows and  
624 unknowns’, *Environmental Chemistry*, 6, pp. 95–105. <https://doi.org/10.1071/EN09007>.

625 Goldberg, T. *et al.* (2009) ‘Mo isotope fractionation during adsorption to Fe  
626 (oxyhydr)oxydes’, *Geochimica et Cosmochimica Acta*, 73, pp. 6502–6516.  
627 <https://doi.org/10.1016/j.gca.2009.08.004>.

628 Gueguen, B. *et al.* (2018) ‘Variable Ni isotope fractionation between Fe-oxyhydroxides and  
629 implications for the use of Ni isotopes as geochemical tracers’, *Chemical Geology*, 481, pp.  
630 38–52. <https://doi.org/10.1016/j.chemgeo.2018.01.023>.

631 Guo, W. *et al.* (2018) ‘Environmental geochemical and spatial/temporal behavior of total and  
632 speciation of antimony in typical contaminated aquatic environment from Xikuangshan,  
633 China’, *Microchemical Journal*, 137, pp. 181–189.  
634 <https://doi.org/10.1016/j.microc.2017.10.010>.

635 Guo, X. *et al.* (2014) ‘Adsorption of antimony onto iron oxyhydroxides: Adsorption behavior  
636 and surface structure’, *Journal of Hazardous Materials*, 276, pp. 339–345.  
637 <http://dx.doi.org/10.1016/j.jhazmat.2014.05.025>.

638 Hao, C. *et al.* (2021) ‘Contrasting water–rock interaction behaviors of antimony and arsenic in  
639 contaminated rivers around an antimony mine, Hunan Province, China’, *Geochemistry*, 81(2),  
640 p. 125748. <https://doi.org/10.1016/j.chemer.2021.125748>.

641 He, M. *et al.* (2019) ‘Antimony speciation in the environment: Recent advances in  
642 understanding the biogeochemical processes and ecological effects’, *Journal of*  
643 *Environmental Sciences*, 75, pp. 14–39. <https://doi.org/10.1016/j.jes.2018.05.023>.

644 Johnson, T. M., *et al.* (2022) ‘A review of the development of Cr, Se, U, Sb, and Te isotopes  
645 as indicators of redox reactions, contaminant fate, and contaminant transport in aqueous  
646 systems’, *Isotopic Constraints on Earth System Processes*, pp. 237–269.

647 Johnston, S. G., *et al.* (2020) ‘Antimony and arsenic speciation, redox-cycling and contrasting  
648 mobility in a mining-impacted river system’, *Science of the Total Environment*, 710, p.  
649 136354. <https://doi.org/10.1016/j.scitotenv.2019.136354>

650 Juillot, F. *et al.* (2008) ‘Zn isotopic fractionation caused by sorption on goethite and 2-Lines  
651 ferrihydrite’, *Geochimica et Cosmochimica Acta*, 72(19), pp. 4886–4900.  
652 <https://doi.org/10.1016/j.gca.2008.07.007>.

653 Komárek, M. *et al.* (2021) ‘Metal isotope complexation with environmentally relevant  
654 surfaces: Opening the isotope fractionation black box’, *Critical Reviews in Environmental*  
655 *Science & Technology*, pp. 1–31. <https://doi.org/10.1080/10643389.2021.1955601>.

656 Leuz, A.-K., Mönch, H. and Johnson, A. (2006) ‘Sorption of Sb(III) and Sb(V) to Goethite:  
657 Influence on Sb(III) Oxidation and Mobilization’, *Environmental Science & Technology*,  
658 40(23), pp. 7277–7282. <https://doi.org/10.1021/es061284b>.

659 Li, S. *et al.* (2021) ‘A new purification method based on a thiol silica column for high  
660 precision antimony isotope measurements’, *Journal of Analytical Atomic Spectrometry*, 36,  
661 pp. 157–164. <https://doi.org/10.1039/D0JA00367K>.

662 Li, Y. *et al.* (2016) ‘Removal of antimonate and antimonite from water by schwertmannite  
663 granules’, *Desalination and Water Treatment*, pp. 1–14.  
664 <https://doi.org/10.1080/19443994.2016.1155176>.

665 Liu, F. *et al.* (2015) ‘Schwertmannite Synthesis through Ferrous Ion Chemical Oxidation  
666 under Different H<sub>2</sub>O<sub>2</sub> Supply Rates and Its Removal Efficiency for Arsenic from  
667 Contaminated Groundwater’, *PLOS ONE*, 10(9), p. e0138891.  
668 <https://doi.org/10.1371/journal.pone.0138891>.

669 Liu, J. *et al.* (2020) ‘Chromatographic purification of antimony for accurate isotope analysis  
670 by MC-ICP-MS’, *Journal of Analytical Atomic Spectrometry*, 35, pp. 1360–1367.  
671 <https://doi.org/10.1039/D0JA00136H>.

- 672 Lobo, L. *et al.* (2012) ‘Investigation of natural isotopic variation of Sb in stibnite ores via  
673 multi-collector ICP-mass spectrometry - perspectives for Sb isotopic analysis of Roman  
674 glass’, *Journal of Analytical Atomic Spectrometry*, 27, pp. 1304–1310.  
675 <https://doi.org/10.1039/c2ja30062a>.
- 676 Lobo, L. *et al.* (2013) ‘Isotopic analysis of antimony using multi-collector ICP-mass  
677 spectrometry for provenance determination of Roman glass’, *Journal of Analytical Atomic  
678 Spectrometry*, 28, pp. 1213–1219. <https://doi.org/10.1039/c3ja50018g>.
- 679 Lobo, L. *et al.* (2014) ‘Copper and antimony isotopic analysis via multi-collector ICP-mass  
680 spectrometry for provenancing ancient glass’, *Journal of Analytical Atomic Spectrometry*,  
681 29(1), pp. 58–64. <https://doi.org/10.1039/C3JA50303H>.
- 682 Manaka, M. *et al.* (2007) ‘Natural attenuation of antimony in mine drainage water’,  
683 *Geochemical Journal*, 41(1), pp. 17–27. <https://doi.org/10.2343/geochemj.41.17>.
- 684 McComb, K.A., Craw, D. and McQuillan, A.J. (2007) ‘ATR-IR Spectroscopic Study of  
685 Antimonate Adsorption to Iron Oxide’, *Langmuir*, 23(24), pp. 12125–12130.  
686 <https://doi.org/10.1021/la7012667>.
- 687 Mitsunobu, S. *et al.* (2010) ‘Antimony(V) Incorporation into Synthetic Ferrihydrite, Goethite,  
688 and Natural Iron Oxyhydroxides’, *Environmental Science & Technology*, 44(10), pp. 3712–  
689 3718. <https://doi.org/10.1021/es903901e>.
- 690 Mitsunobu, S., Harada, T. and Takahashi, Y. (2006) ‘Comparison of Antimony Behavior with  
691 that of Arsenic under Various Soil Redox Conditions’, *Environmental Science & Technology*,  
692 40(23), pp. 7270–7276. <https://doi.org/10.1021/es060694x>.
- 693 Nagano, T. *et al.* (2011) ‘Evaluation of the Affinity of Some Toxic Elements to  
694 Schwertmannite in Natural Streams Contaminated with Acid Mine Drainage’, *Water, Air, &  
695 Soil Pollution*, 216(1), pp. 153–166. <https://doi.org/10.1007/s11270-010-0523-9>.
- 696 Parks, G.A. (1965) ‘The isoelectric points of solid oxides, solid hydroxides, and aqueous  
697 hydroxo complex systems’, *Chemical Reviews*, 65(2), pp. 177–198.  
698 <https://doi.org/10.1021/cr60234a002>
- 699 Pokrovsky, O.S. *et al.* (2014) ‘Germanium isotope fractionation during Ge adsorption on  
700 goethite and its coprecipitation with Fe oxy(hydr)oxides’, *Geochimica et Cosmochimica Acta*,  
701 131, pp. 138–149. <https://doi.org/10.1016/j.gca.2014.01.023>.
- 702 Qi, P. and Pichler, T. (2016) ‘Sequential and simultaneous adsorption of Sb(III) and Sb(V) on  
703 ferrihydrite: Implications for oxidation and competition’, *Chemosphere*, 145, pp. 55–60.  
704 <https://doi.org/10.1016/j.chemosphere.2015.11.057>.
- 705 Qi, P. and Pichler, T. (2017) ‘Competitive adsorption of As(III), As(V), Sb(III) and Sb(V)  
706 onto ferrihydrite in multi-component systems: Implications for mobility and distribution’,  
707 *Journal of Hazardous Materials*, 330, pp. 142–148.  
708 <https://doi.org/10.1016/j.jhazmat.2017.02.016>.

709 Regenspurg, S., Brand, A. and Peiffer, S. (2004) 'Formation and stability of schwertmannite  
710 in acidic mining lakes', *Geochimica et Cosmochimica Acta*, 68(6), pp. 1185–1197.  
711 <https://doi.org/10.1016/j.gca.2003.07.015>.

712 Rastegari, M., et al. (2022). Antimony (V) incorporation into schwertmannite: critical insights  
713 on antimony retention in acidic environments. *Environmental science & technology*, 56(24),  
714 17776-17784

715 Resongles, E. *et al.* (2013) 'Fate of Sb(V) and Sb(III) species along a gradient of pH and  
716 oxygen concentration in the Carnoulès mine waters (Southern France)', *Environmental*  
717 *Science Processes and Impacts*, 15, pp. 1536–1544. <https://doi.org/10.1039/c3em00215b>.

718 Resongles, E. *et al.* (2015) 'Antimony isotopic composition in river waters affected by ancient  
719 mining activity', *Talanta*, 144, pp. 851–861. <http://dx.doi.org/10.1016/j.talanta.2015.07.013>.

720 Resongles, E. *et al.* (2021) 'Antimony isotopic composition in stream waters impacted by acid  
721 mine drainage', *Goldschmidt2021*, Virtual, 4-9 July 2021.  
722 <https://doi.org/10.7185/gold2021.5268>

723 Rouxel, O., Ludden, J. and Fouquet, Y. (2003) 'Antimony isotope variations in natural  
724 systems and implications for their use as geochemical tracers', *Chemical Geology*, 200, pp.  
725 25–40. [https://doi.org/10.1016/S0009-2541\(03\)00121-9](https://doi.org/10.1016/S0009-2541(03)00121-9).

726 Scheinost, A.C. *et al.* (2006) 'Quantitative antimony speciation in shooting-range soils by  
727 EXAFS spectroscopy', *Geochimica et Cosmochimica Acta*, 70(13), pp. 3299–3312.  
728 <https://doi.org/10.1016/j.gca.2006.03.020>.

729 Schoepfer, V. A., & Burton, E. D. (2021) 'Schwertmannite: a review of its occurrence,  
730 formation, structure, stability and interactions with oxyanions', *Earth-Science Reviews*, 221,  
731 p. 103811. <https://doi.org/10.1016/j.earscirev.2021.103811>.

732 Schwertmann, U. and Cornell, R.M. (2000) *Iron Oxides in the Laboratory - Preparation and*  
733 *characterization*. Second Edition. WILEY-VCH.

734 Shan, J., *et al.* (2023). Antimony immobilization mechanism on schwertmannite: Insights  
735 from the microstructure of schwertmannite. *Geochimica et Cosmochimica Acta*, 359, 71-83.

736 Sun, G. *et al.* (2021) 'Precise analysis of antimony isotopic composition in geochemical  
737 materials by MC-ICP-MS', *Chemical Geology*, 582, p. 120459.  
738 <https://doi.org/10.1016/j.chemgeo.2021.120459>.

739 Tanimizu, M. *et al.* (2011) 'Determination of natural isotopic variation in antimony using  
740 inductively coupled plasma mass spectrometry for an uncertainty estimation of the standard  
741 atomic weight of antimony', *Geochemical Journal*, 45, pp. 27–32.

742 Tella, M., & Pokrovski, G. S. (2012) 'Stability and structure of pentavalent antimony  
743 complexes with aqueous organic ligands', *Chemical Geology*, 292, pp. 57-68.

744 Teng, F.-Z., Dauphas, N. and Watkins, J.M. (2017) 'Non-Traditional Stable Isotopes:  
745 Retrospective and Prospective', *Reviews in Mineralogy and Geochemistry*, 82(1), pp. 1–26.  
746 <https://doi.org/10.2138/rmg.2017.82.1>.

747 U.S. Geological Survey (2018) ‘Antimony - Historical Statistics (Data series 140 - 2018  
748 update)’. Available at: [https://www.usgs.gov/media/files/antimony-historical-statistics-data-](https://www.usgs.gov/media/files/antimony-historical-statistics-data-series-140)  
749 [series-140](https://www.usgs.gov/media/files/antimony-historical-statistics-data-series-140). Last access on 27/7/2023.

750 U.S. Geological Survey (2022) *2022 Final List of Critical Minerals*. Notices Federal Register  
751 / Vol. 87, No. 37.

752 Veldhuizen, H.J., MacKinney, J.S., Johnson, T.M. ‘Kinetic Fractionation of Antimony  
753 Isotopes during Reduction by Sulfide.’ *ACS Earth Space Chem.* **7** (2023): 2603–2612.  
754 <https://doi.org/10.1021/acsearthspacechem.3c00269>

755 Wang, S.-J. and Wasylenki, L.E. (2017) ‘Experimental constraints on reconstruction of  
756 Archean seawater Ni isotopic composition from banded iron formations’, *Geochimica et*  
757 *Cosmochimica Acta*, 206, pp. 137–150. <https://doi.org/10.1016/j.gca.2017.02.023>.

758 Wang, X. *et al.* (2011) ‘Antimony distribution and mobility in rivers around the world’s  
759 largest antimony mine of Xikuangshan, Hunan Province, China’, *Microchemical Journal*,  
760 97(1), pp. 4–11. <https://doi.org/10.1016/j.microc.2010.05.011>.

761 Wasylenki, L.E. *et al.* (2011) ‘The molecular mechanism of Mo isotope fractionation during  
762 adsorption to birnessite’, *Geochimica et Cosmochimica Acta*, 75(17), pp. 5019–5031.  
763 <https://doi.org/10.1016/j.gca.2011.06.020>.

764 Wasylenki, L.E. *et al.* (2015) ‘Ni isotope fractionation during sorption to ferrihydrite:  
765 Implications for Ni in banded iron formations’, *Chemical Geology*, 400, pp. 56–64.  
766 <https://doi.org/10.1016/j.chemgeo.2015.02.007>.

767 WHO, World Health Organization (2011) ‘Fourth Edition. Guidelines for drinking-water  
768 quality

769 WHO Chronicle’, 38 (4), pp. 104-108.

770 Wiederhold, J.G. (2015) ‘Metal Stable Isotope Signatures as Tracers in Environmental  
771 Geochemistry’, *Environmental Science & Technology*, 49(5), pp. 2606–2624.  
772 <https://doi.org/10.1021/es504683e>.

773 Wu, D., Pichler, T. (2016) ‘Preservation of co-occurring As, Sb and Se species in water  
774 samples with EDTA and acidification’, *Geochemistry: Exploration, Environment, Analysis*,  
775 16, p.p. 117–125. <https://doi.org/10.1144/geochem2015-369>.

776 Xu, W. *et al.* (2020) ‘Selenium isotope fractionation during adsorption by Fe, Mn and Al  
777 oxides’, *Geochimica et Cosmochimica Acta*, 272, pp. 121–136.  
778 <https://doi.org/10.1016/j.gca.2020.01.001>.

779 Yan, X. *et al.* (2021) ‘Cadmium Isotope Fractionation during Adsorption and Substitution  
780 with Iron (Oxyhydr)oxides’, *Environmental Science & Technology*, 55(17), pp. 11601–11611.  
781 <https://doi.org/10.1021/acs.est.0c06927>.

782 Zhou, W. *et al.* (2022) ‘Antimony isotope fractionation during adsorption on aluminum  
783 oxides’, *Journal of Hazardous Materials*, 429, p. 128317.  
784 <https://doi.org/10.1016/j.jhazmat.2022.128317>.

785 Zhou, W. *et al.* (2023) ‘Antimony Isotope Fractionation Revealed from EXAFS during  
786 Adsorption on Fe (Oxyhydr)oxides’, *Environmental Science & Technology*, 57, pp.  
787 9353–9361. <https://doi.org/10.1021/acs.est.3c01906>